Chapter 6
Femtosecond Laser Ablation: Fundamentals and Applications

Sivanandan S. Harilal, Justin R. Freeman, Prasoon K. Diwakar and Ahmed Hassanein

Abstract Traditionally nanosecond laser pulses have been used for Laser-induced Breakdown Spectroscopy (LIBS) for quantitative and qualitative analysis of the samples. Laser produced plasmas using nanosecond laser pulses have been studied extensively since 1960s. With the advent of short and ultrashort laser pulses, there has been a growing interest in the applications of femtosecond and picosecond lasers for analysis of materials using LIBS and LA-ICP-MS. The fundamentals of laser ablation process using ultrashort laser pulses are not still fully understood. Pulse duration of femtosecond laser pulse is shorter than electron-to-ion energy transfer time and heat conduction time in the sample lattice. This results in different laser ablation and heat dissipation mechanisms as compared to nanosecond laser ablation. In this chapter, the focus will be on understanding the basics of femtosecond laser ablation processes including laser target interaction, ablation efficiency, ablation threshold, laser plasma interactions, and plume hydrodynamics. Analytical figures of merit will be discussed in contrast to nanosecond LIBS.

6.1 Introduction

Laser ablation (LA) and laser-produced plasmas (LPP) have been studied extensively for more than 50 years since the discovery of lasers in the 1960s. The physics involved in laser-plasma generation and subsequent evolution is very complex and contains many processes like heating, melting, vaporization, ejection of particles, and plasma creation and expansion. The laser ablation craters and plasmas produced are dependent on laser beam parameters such as pulse duration, energy, and wavelength, along with the target properties and surrounding

S. S. Harilal (✉) · J. R. Freeman · P. K. Diwakar · A. Hassanein
Center for Materials Under Extreme Environment, School of Nuclear Engineering, Purdue University, West Lafayette, IN 47907, USA
e-mail: hari@purdue.edu

S. Musazzi and U. Perini (eds.), *Laser-Induced Breakdown Spectroscopy*,
Springer Series in Optical Sciences 182, DOI: 10.1007/978-3-642-45085-3_6,

conditions. Many of the present applications of LPP have been developed in the past using nanosecond pulsed lasers by industry along with defense programs. Two of the well-known analytical applications of laser ablation are laser-induced breakdown spectroscopy (LIBS) and laser-ablation inductively coupled plasma mass spectrometry (LA-ICP-MS). LIBS is a technique commonly used to identify constituents of an unknown sample by ablating a small amount of the sample and studying the resultant optical emission. LA-ICP-MS is a complementary technique where the ablated mass is analyzed for elemental and isotope detection, compared to detection through analysis of light emission in LIBS.

In LIBS, a high power laser is used for ablation, typically nanosecond (ns) Q-switched lasers, and subsequent light emission is collected and dispersed using a spectrograph. The detection is performed either using a time-integrated CCD or an intensified CCD (ICCD). In fact, the first LIBS experiments were performed immediately after the invention of the first laser and recently the 50th anniversary of LIBS was celebrated during the LIBS 2012 conference held in Luxor, Egypt. The advancements in LIBS in the last three decades are mainly due to availability of relatively inexpensive, compact and stable ns Nd:YAG lasers, improvement in the performance of spectrographs (e.g., miniaturized spectrographs, Echelle, etc.), and sensitive light detection systems (ICCD).

As with all laser ablation, the properties of the LIBS plasma and its emission are strongly dependent on laser parameters such as pulse length and wavelength. Laser wavelength affects the penetration of laser radiation into a target, either solid or plasma, affecting where energy is deposited and where heating occurs. Shorter wavelengths are preferable for LA-ICP-MS since it provides higher photon energies for bond breaking (molecule dissociation) and reduced fractionation. Moreover, because of higher critical density, the laser-target coupling will be higher for UV wavelengths compared to IR wavelengths [1, 2]. However, most of the LIBS research and analysis has been performed using 1064 nm radiation from ns Nd:YAG lasers.

Traditionally nanosecond laser pulses have been used for LIBS and LA-ICP-MS for quantitative and qualitative analysis of the samples, but with the advent of short and ultrashort laser pulses, there has been a growing interest in the applications of femtosecond (fs) lasers for analysis of materials using LIBS and LA-ICP-MS. The laser–matter interaction and the mechanisms leading to ablation are dissimilar for different laser pulse widths. In this chapter, the focus will be on understanding the basics of femtosecond laser ablation processes which include laser energy transport, ablation mechanisms, ablation threshold, plume hydrodynamics and evolution. In particular, a comprehensive comparison between the ns and fs laser ablation mechanisms, plasma formation and their evolution is discussed. This chapter begins with a brief description of fs laser physics and diagnostic needs, followed by details of laser-target coupling, ablation mechanisms, ablation threshold, and plume characterization.

6.2 Femtosecond Laser System

The field of laser ablation and its applications has been growing since the development of the laser in the 1960s. However, the peak intensity achievable from the early laser sources stagnated development for more than three decades. This scenario changed dramatically with the invention of chirped pulsed amplification (CPA) [3] that stretches the laser pulse in time prior to the amplification and the discovery of high fluence solid state materials like Ti–Sapphire led to revolutionary developments in the peak power of table-top lasers. In fact, the idea of CPA revolutionized high power lasers and their applications in science and technology and as well as in industry. The idea of CPA was indeed significant and simple. The concept of CPA is given in Fig. 6.1. In CPA, the laser pulses are temporally manipulated in a controllable and reversible fashion so that the optics in the amplifier never encounter high peak power. It should be noted that the major challenges associated with high peak power in the pre-CPA era was optical damage induced by high power lasers. In order to overcome such high beam intensity limitations, large aperture laser amplifiers were used which are very inefficient and bulky.

Currently, most of the commercially available femtosecond (fs) laser systems use CPA technology. Commercially available CPA-based fs laser systems consist of an oscillator, stretcher, amplifier and compressor (Fig. 6.1). The oscillator, or seed laser, typically a mode-locked Ti–Sapphire laser, provides a train of fs pulses emitting around 800 nm, and a few nJ of energy at high repetition rate ($\sim$75 MHz). These pulses will be temporally stretched (to ps-ns duration) before amplification. The amplified pulse will be compressed back to its original pulse duration in a pulse compressor. The recompressed pulse output from a CPA system exhibits peak powers that are usually not producible in long-pulse lasers. However, a CPA-based laser system carries much less energy even though it provides high peak intensities.

Using CPA technology, high peak power is obtained in laboratories by shortening the laser pulse rather than increasing the energy to higher levels, and a new vibrant discipline 'ultrafast optics' has emerged [4]. Ultrafast regime implies the use of lasers with CPA technology which emit pulses of $\sim$10 s of femtoseconds. Such a short time scale is equivalent to the time over which an electron circulates around an atom (atomic or quantum time). Although these lasers are not producing very high energies, the power exceeds terawatts because of shorter pulse width. If we focus these beams to a minute spot size ($\sim$10 μm), massive intensity in the range of 10^{18} Wcm^{-2} or higher is possible, corresponding to an electric field $\sim 10^{11}$ V/cm. Such huge laser intensity opens up new regimes of physics under extreme conditions, commonly called high energy density physics (HEDP) [5]. For example, the plasmas generated by such a laser emit high energy electrons leading to bright emission of electrons, x-rays, and γ-rays [6]. The nonlinear interaction of an intense femtosecond laser pulse with matter may lead to the emission of a train of sub-laser-cycle-attosecond-bursts of short-wavelength radiation (harmonic

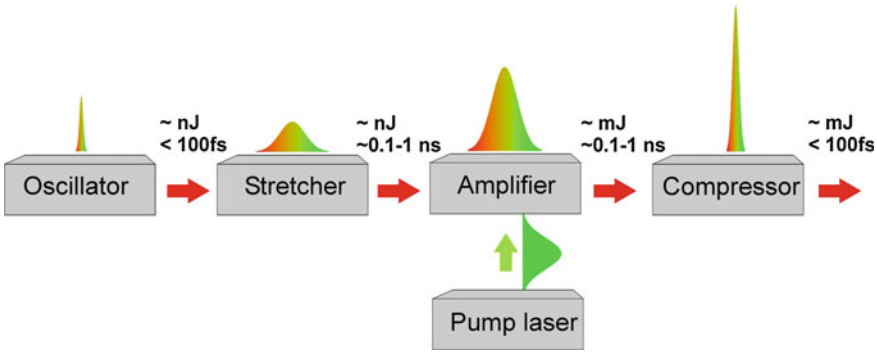

Fig. 6.1 Schematic of chirped pulsed amplification (CPA) based laser system

generation) [7]. Such a hyper fast-varying electric field of laser light will permit manipulation and tracking of the atomic-scale motion of electrons.

The recent developments in fs laser technology stimulated a new field of ultrafast LIBS, or fs LIBS. The main difference of fs LIBS with respect to traditional LIBS is the use of an ultrafast laser for excitation. However, the use of fs lasers in ultrafast LIBS warrants more diagnostic needs on the laser side compared to ns laser-based LIBS. The pre-pulse from the fs laser system and the temporal pulse change or chirp when it passes through a refractive medium have to be monitored carefully. If the contrast of the fs laser system (ratio of the peak pulse to the pre-pulse or background) is poor, the pre-pulses can induce deleterious effects during laser-target interaction [8]. The intensity contrast ratio should be $\geq 10^6$ for 100 fs laser main pulse with ns pre-pulse for avoiding pre-pulse damage to the material. The origin of pre-pulses in fs laser systems are due to incorrect recompression of the stretched pulses, leakage from the Pockels cells in the regenerative amplifier, or an amplified spontaneous emission (ASE) background. Since the fs laser pulses are inherently broadband, the beam is susceptible to group velocity dispersion (GVD) when it passes through a refractive medium [4]. GVD introduces a frequency dependent delay of the spectral components of the pulse leading to broadening of the pulse in time. GVD and associated group delay dispersion (GDD) are relevant considerations for pulses with width $\leq$50 fs, but less significant for pulses $\geq$100 fs.

For ns pulse duration, the laser propagation through media is negligibly influenced by the media properties. However, for fs duration, nonlinear absorption becomes significant in all materials, including air. If the femtosecond laser intensity is higher than the critical power for self-focusing, filamentation can occur in the beam [9]. However, the laser energy required for laboratory ultrafast LIBS is not very high ($\leq$1 mJ), and the probability of filamentation in the beam path is negligible. However, filamentation can occur during the focusing of the beam at the target surface. Therefore, for ultrafast LIBS, it is essential to keep the focal point just behind the target for avoiding filamentation in air. There is a positive

aspect of filamentation considering LIBS experiments. Filamentation in air can be manipulated to occur for distances as far as few kilometers, making it ideally suited for remote sensing [10]. Currently, many efforts are ongoing to develop filamentation-based LIBS for remote sensing [11–13].

Finally, it has to be mentioned that the availability of user-friendly ultrafast lasers is pivotal to their widespread use in scientific research and industry. Femtosecond laser technology has already made unprecedented advancements in the last decade leading to more compact, reliable, and user-friendly systems. The availability of turn-key femtosecond fiber lasers will supplement their deployments in a wide and varied range of applications, including LIBS [14].

6.3 Laser–Matter Interaction

Even though the only difference between the conventional ns laser based LIBS and ultrafast LIBS is the difference in laser system, the mechanisms leading to energy absorption and target ablation are entirely different for both cases. Approximate time scales of nanosecond and femtosecond energy absorption and laser ablation, along with various processes happening during and after the laser pulse, are given in Fig. 6.2 [15–17]. The differences between ns and fs laser ablation mechanisms are drastic due to the significant differences in laser pulse length. Whereas ionization, sample heating, and vaporization all occur during the laser pulse in ns laser ablation, fs laser pulses are so short that these phenomena do not occur until the end or after the laser pulse. Femtosecond pulse duration is shorter than the characteristic relaxation times, such as the electron-to-ion energy transfer time, electron heat conduction time, and hence the hydrodynamic or expansion time; all of which typically occur on the order of several picoseconds after laser absorption. Because of this, ultrafast LIBS offers greatly reduced thermal damage and heat-affected zone (HAZ) in the target due to negligible heat conduction and hydrodynamic motion during the laser pulse duration. Moreover, the spatial resolution obtained by fs pulses is better than ns pulses. Recent studies showed that submicron scale fs laser ablation can be carried out for chemical analysis [18].

Apart from pulse duration, laser wavelength affects the laser ablation properties, especially in ns LA. Previous studies showed that laser wavelength affects laser-target (mass ablation rate, penetration depth) and laser-plasma (absorption, reflection) coupling efficiencies, as well as optical properties of the plasma (opacity) [1, 19]. This is due to reduced plasma shielding and enhanced laser-target coupling at shorter wavelengths caused by higher critical density of the plasma [20, 21]. Therefore, shorter wavelengths are preferable in ns-LA for the introduction of a more representative and greater quantity of aerosol into the ICP-MS, which in turn will lower fractionation effects. However, the role of fs wavelength on laser ablation and elemental fractionation is not well understood. In fact, it is a controversial subject and fs wavelengths are thought to have little influence in

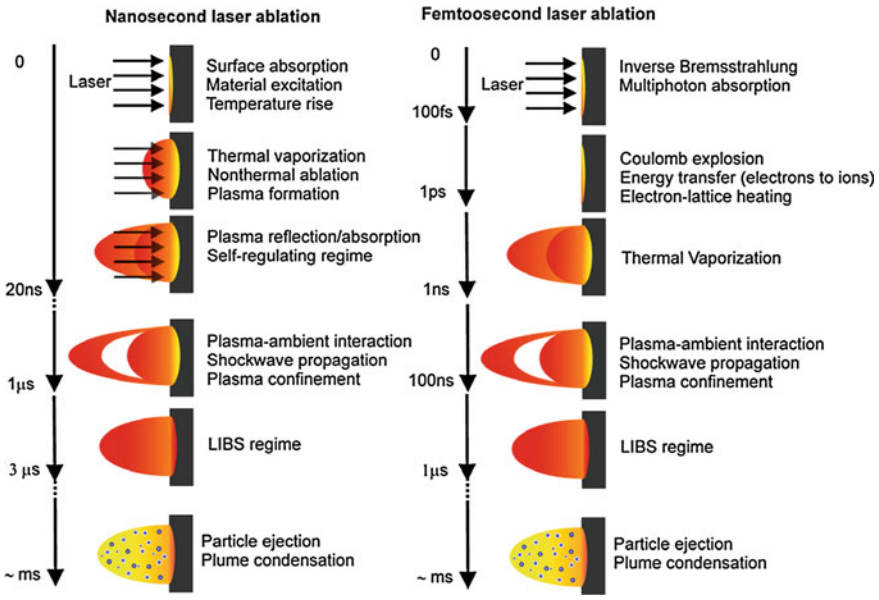

Fig. 6.2 Approximate time scales of nanosecond and femtosecond energy absorption and laser ablation along with various processes happening during and after the laser pulse is given

laser ablation due to significantly shorter duration of the laser pulse compared to electron to ion energy transfer time and heat conduction time [22].

The physical mechanisms behind ionization and material removal in fs-LA are debated and not well understood. Even though a complete physical model of fs laser–matter interaction has thus far puzzled researchers, the entire process can be subdivided into photon energy absorption by electrons and redistribution of absorbed energy to lattice and ions, leading to ablation. The details of fs laser absorption and subsequent ablation processes are given in the Sects. 6.4 and 6.5.

6.4 Femtosecond Laser Absorption: Energy Transport

During laser–matter interaction, regardless of the pulse duration, the laser photon energy will be coupled to the electrons in the system. There are significant differences between the energy absorption and ablation processes for ultra-fast ($\sim$<1 ps) and short ($\sim$>1 ps) laser ablation. For long pulse ns lasers, the absorption process is linear and obeys the Beer-Lambert law. However, because of high peak intensities, nonlinear processes become significant during ultrafast laser absorption. The electron impact ionization and strong electric field ionization (photoionization) are the major processes for free electron generation during fs laser ablation. It has to be pointed out that the absorption processes, as well as

ablation physics, will be different for metals and dielectrics. For example, in metals free electrons in the conduction band absorb energy through inverse Bremsstrahlung absorption. For dielectrics, valence band electrons absorb photons and if they do not have enough energy to reach the next energy level in the conduction band the electrons generally decay to their initial state and reemit the photon. This is the case for ns and ps laser absorption in dielectrics and explains why ablation of dielectrics requires much higher laser intensities.

During fs laser interaction with materials, the photon energy will be transferred to the electrons. If a free electron's kinetic energy is sufficiently high enough after photon absorption, it can transfer energy to a bound electron during collision to overcome the ionization potential. This process is called electron impact ionization. Electron impact ionizations are able to double the number of free electrons and after a series of collisions and photon energy absorptions, what is referred to as an electron avalanche occurs.

At higher laser intensities, especially above 10^{13} Wcm^{-2}, strong electric field ionization or photoionization becomes significant. Depending upon the laser intensity, different strong electric field ionization processes may happen that include multi-photon ionization (MPI) and tunnel ionization (TI). In the case of dielectrics, if the photon flux is high enough, several (n) photons can be absorbed by one electron before it decays back to its initial state. If the combined energy of these absorbed photons, $nh\upsilon$, is greater than the energy difference between the valence and conduction bands, referred to as the band gap, then the electron will be excited into the conduction band. In MPI, the bound electron is freed when the combined energy of n photons ($nh\upsilon$) absorbed exceeds the ionization potential. At extremely high intensities (10^{15} Wcm^{-2}), tunnel ionization becomes stronger. In TI, the strong electric field created by the laser distorts the band structure and reduces the potential barrier between the valance and conduction bands. The power densities typically used in fs-LIBS or in fs LA-ICP-MS is $<10^{15}$ W/cm^2 and hence tunnel ionization is not expected to be significant.

For dielectrics, impact ionization requires sufficient number of high-energy electrons present in the conduction band. Therefore, impact ionization starts much later than the strong field ionization. The seed electrons for impact ionization may be provided by MPI or TI. Kaiser et al. [23] investigated the role of strong electric field ionization and electron impact ionization using time dependent Boltzmann equations when a dielectric material was irradiated with fs laser pulses with an electric field of 150 MV/cm with various pulse durations (25–200 fs). Their results showed that (Fig. 6.3) avalanche ionization is negligible for laser durations below 100 fs, where photoionization is dominant, and the free electron density by impact ionization becomes as important as strong field ionization only when the pulse width is $\sim$200 fs.

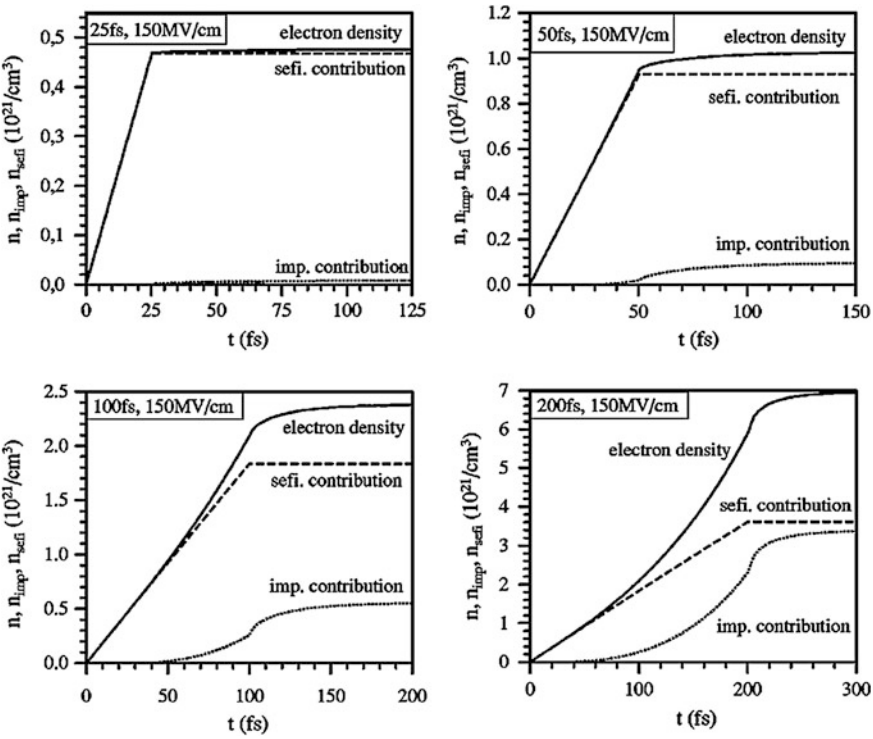

Fig. 6.3 Time dependent free electron density contribution for strong electric field ionization and impact ionization for fs laser pulses with durations 25, 50, 100 and 200. For obtaining these results a SiO_2 target was irradiated with a 500 nm, 150 MV/cm laser pulse (After Kaiser et al. [23])

6.5 Ablation Mechanisms

Laser ablation is defined as the removal of the material from a target of interest by direct absorption of laser energy. Plasma formation occurs when a high-powered pulsed laser is focused onto a target such that the energy density surpasses the ablation threshold of the material. For long pulse ns laser ablation, the dissipation of absorbed energy in the bulk material and the material removal takes place during the laser pulse duration. However, for ultrafast laser ablation, the duration of the laser pulse is shorter than the characteristic relaxation times, such as the electron-to-ion energy transfer time and electron heat conduction time and hence, the hydrodynamic or expansion time. All of these typically occur on the order of several picoseconds after laser absorption (see the time scales given in Fig. 6.2). Hence, for laser pulses of picoseconds or shorter, heat diffusion is *frozen* during the interaction of the laser beam with material and the shock-like energy deposition leads to ablation.

For fs laser pulses, there are two competing mechanisms resulting in material removal and ablation: the Coulomb explosion (gentle ablation) and thermal vaporization (strong ablation). The Coulomb explosion dominates at low laser intensities near the ablation threshold. Excited electrons are ejected from the target surface, creating an electric field of charge separation between the ejected electrons and the highly ionized atoms at the target surface, referred to as the space-charge effect. Charge separation occurs if the energy absorbed by electrons exceeds the Fermi energy, which can be considered the sum of the electron binding energy (for dielectrics) and work function, allowing electrons to escape from the target. If the electron energy is greater than the binding energy of the ions in the lattice, the resultant electric field pulls the ions out of the target, resulting in removal of the first few monolayers (several nanometers) of the lattice within the skin depth. At sufficiently high laser intensities above the ablation threshold, the phase explosion is followed by thermal vaporization of the bulk material becomes the dominant mechanism for material removal.

There are distinct differences in ablation regimes between Coulomb explosion and thermal vaporization. In Coulomb explosion a few nm in depth is removed per pulse and leaves behind a smoother surface, while for thermal vaporization, an order of magnitude higher ablation rate per pulse is removed. Figure 6.4 shows the differences in craters after gentle and strong ablation phases obtained by Stoian et al. [24] and they noticed these processes depended strongly on number of laser pulses hitting at the target surface. The velocities of the ions are found to be significantly higher and similar momenta for all ions of different materials are exhibited in the case of Coulomb explosion, in contrast to thermal vaporization, where ions have similar kinetic energy. Ablated material under the thermal vaporization regime is of comparable temperature to the vaporization temperature of the material. Ion flux and kinetic energy studies also show fs laser plasmas produce narrower angular distributions while ns laser plasmas provide narrower energy distribution [25].

Several authors reported a double-peak time-of-flight (TOF) distribution for ions and electrons during ultrafast laser ablation [25–28]. Amoruso et al. [26, 29] have observed a double-peak distribution of emitted ions and electrons during ultrafast laser ablation, concluding that the first, high-energy component might be non-thermal and could be explained by the space-charge effect, followed by the second peak, consisting of thermalized ions and electrons. They noticed a strong power law dependence on laser pulse intensity for the fast ion component, which is much stronger than the logarithmic dependence of the slow component, indicating the fast component is of non-thermal nature. Zhang et al. [28] have identified the fast ions due to highly-charged species, with mostly singly- and doubly-charged ions contributing to the slower component. These characteristics of the fast ions lead one to identify them as the result of the space-charge effect occurring during Coulomb explosion, while the slower ions are those thermalized in the target and ejected by thermal vaporization. Thermal vaporization also results in the ejection of neutral atoms from the target. The two ablation mechanisms result in a plasma layer of energetic electrons and faster, higher-charged ions ejected from the target,

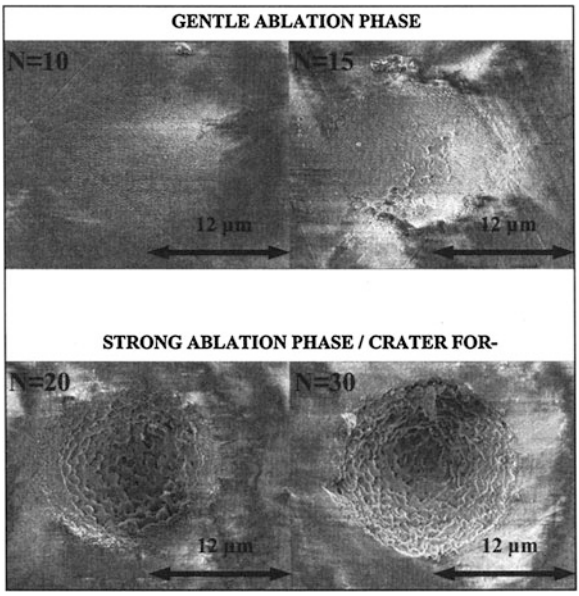

Fig. 6.4 SEM pictures of fs laser irradiated spot of Al_2O_3 after different number of pulses at the target surface. Smooth and rough crater surfaces were obtained after Coulomb explosion (gentle ablation) and thermal vaporization (strong ablation), respectively (After Stoian et al. [24])

followed by the core of the plasma undergoing hydrodynamic expansion away from the target and consisting of mostly neutral atoms, electrons, and slower, lower-charged ions.

6.6 Ablation Threshold

Laser ablation typically exhibits a threshold behavior with respect to laser fluence: ablation happens only when the laser fluence is greater than a certain value at a given pulse width. Several experimental methods were used for estimating ablation threshold (F_{th}) or laser damage, which include plasma radiation monitoring, photothermal deflection, analysis of craters, visual acquisition, etc. Previous studies showed that $F_{th} \sim \tau_p^{1/2}$ for ns and ps LA, where τ_p is the laser pulse width [30]. However for fs pulses, the electron temperature dominates the electron–phonon temperature and hence, the photon absorption depth governs the heated volume instead of heat diffusion depth (heat diffusion depth is proportional to $\tau_p^{1/2}$). Perry et al. [31] noticed a strong deviation from the usual $\tau_p^{1/2}$ scaling of laser ablation threshold for pulses below 10 ps in dielectric materials (see Fig. 6.5). Gamaly et al. [32] investigated ablation of solids by fs laser pulses theoretically and obtained similar results to Perry et al. [31]. Since the pulse duration in the case of fs pulses is shorter than the heat conduction time (τ_{heat}), the electron to ion energy transfer time, and the plasma expansion time, the fs laser interaction with any material results in ionization. Hence, the interaction of fs lasers with metals

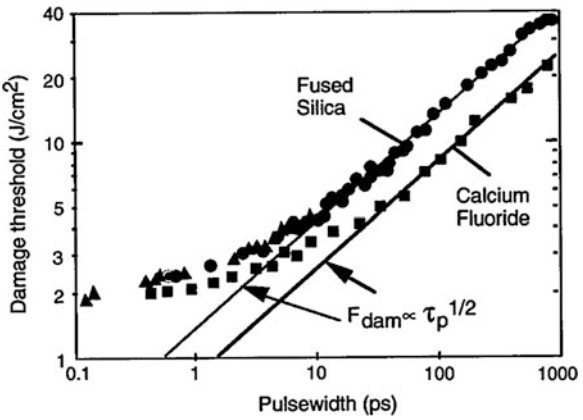

Fig. 6.5 Observed laser ablation threshold values with respect to pulse width for dielectric materials (After Perry et al. [31]). The *solid lines* represent $\tau_p^{1/2}$ fits to long pulse lasers

and dielectrics ensues in a similar manner, in contrast to the interaction between long-pulse lasers with materials. Lenzner et al. [33] reported significant differences between single and multi-shot ablation threshold during 5 fs laser interaction with fused silica and concluded that incubation effects alter the optical properties of the materials. Figure 6.5 also shows the laser fluence required for the fs LA is significantly lower compared to long pulse lasers and hence precise ablation of sample (10–100 nm) is possible opening up the possibility of depth-profiling of multi-layer samples [34].

The differences in ablation mechanisms during interaction between materials with ns and fs lasers constitute distinct differences in their crater shape. Leitz et al. [35] compared the craters formed by lasers with different pulse widths (μs, ns, ps, and fs) and noticed significant differences in crater shape as well as volume. The pulse width-dependent laser beam-material interaction can be broadly classified into two regimes: long ($\tau_p \gg \tau_{heat}$) and short ($\tau_p \ll \tau_{heat}$) pulse ablation. For long pulse ablation, the process is dominated by heat conduction, melting, evaporation and plasma formation and ablation is determined by both evaporation and melt expulsion. Since the time scale of ns laser ablation is comparable to the heat diffusion times, the shock waves propagating through the melt layer and the ablation-induced reactive force initiate splashing of the melt layer.

The ultrafast laser pulse interaction with material and energy transfer to the lattice can be understood from a two-temperature diffusion model. In this model, the electrons that absorb the laser energy are close to the surface and are of one temperature, while the ions immediately below the surface remain at room temperature initially after the ultrafast laser pulse. Because of this, ultrafast laser-induced phase transformations occur in non-equilibrium conditions [36]. Energy transfer from the electrons to the lattice is the result of electron–phonon interactions. The lattice melts a few picoseconds after the laser irradiation, leading to material ablation. Since all these processes happen in a short time scales ($\sim$ps), the heat load to the surrounding material is minimized. Hence, the craters formed by fs laser ablation will be cleaner, with well-defined edges, while the ns laser

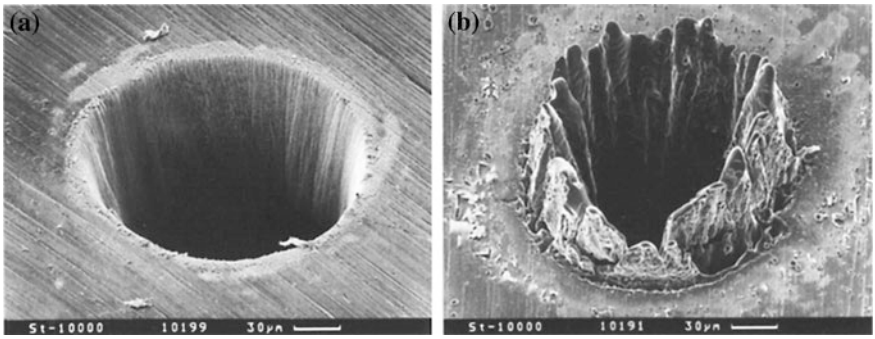

Fig. 6.6 Laser ablation craters in a 100 μm thick steel foil with (**a**) 200 fs, 780 nm and 120 μJ; and (**b**) 3.3 ns, 780 nm and 1 mJ laser pulses (After Chichkov et al. [37])

ablation craters showed significant irregularities in the crater rims because of resolidification of splashed melt layers (Fig. 6.6) [37].

Ultrafast lasers are capable of increased target ablation compared to longer-pulse lasers of similar laser fluence levels. Le Drogoff et al. [38] have demonstrated this using laser pulse durations from 80 fs to 270 ps, with highest ablation volumes achieved with pulse duration shorter than 1 ps. During longer-pulse laser ablation, the beginning of the laser pulse interacts with the target, creating plasma that shields much of the subsequent laser radiation from reaching the target. Most of the laser radiation is then spent reheating the preformed plasma plume, while for ultrafast laser ablation all laser energy is deposited directly onto the target before ablation occurs. This results in more efficient deposition of laser energy onto the target by ultrafast lasers. In the context of LIBS, the amount of material removed and large area heat affected zone must be considered if dealing with delicate samples such as artwork or if detecting trace elements, when increased sampling size may be beneficial.

6.7 Plasma Characterization: Comparison Between ns and fs LIBS Plumes

In the previous sections, the major emphasis was on the fs laser system along with its interaction with materials, energy absorption, ablation mechanisms, crater formation, etc. As mentioned earlier, laser ablation has numerous applications. LIBS and LA-ICP-MS are two well-known analytical applications of laser ablation. Both these analytical techniques are highly sensitive to laser parameters and recent results showed significant improvement in detection limits as well as reduced fractionation using ultrafast laser ablation. There exist a few excellent review papers on this topic [16, 17].

Numerous studies have been conducted in recent years to understand the differences in ns and fs LPP and the overall analytical figures of merit offered by fs LPP for qualitative and quantitative analysis [37, 39–42]. Plasmas produced by ultrafast laser systems have many benefits over typical ns lasers mainly due to $\tau_{ei} \sim \tau_{heat} \gg \tau_p$. The benefits of the shorter pulse are tremendous in micromachining and medical surgery as it provides higher precision during ablation and minimized HAZ to the target material compared to nanosecond lasers [43]. The HAZ of ns laser ablation is typically 100 μm to 1 mm, whereas a negligible HAZ is noticed for fs laser ablation because of the limited penetration length of thermal diffusion. Limited HAZ in fs LIBS also prevents uncontrollable and undesirable material modification and removal as seen with long pulse laser ablation. Femtosecond LA-ICP-MS generates uniform aerosol size distribution and in doing so it reduces elemental fractionation [44]. Ultrafast pulsed laser deposition (PLD) also leads to automatic generation of nanometer-scale particles during ablation [45, 46].

6.7.1 Plume Hydrodynamics

Typically, LIBS experiments are performed in ambient air atmosphere. The presence of ambient air affects the hydrodynamic expansion properties of laser ablation plumes. Figures 6.7 and 6.8 show ICCD time-integrated images of emission in the visible region (350–800 nm) from ns and fs LPPs. Intensities have been normalized to the maximum intensity seen from both figures. We see significant differences in expansion of emitting species between ambient atmosphere and vacuum environments. For the case of ns LPP emission (Fig. 6.7), spherical expansion of the plume is observed. In vacuum, expansion of the emitting species is significant and emission can be seen at distances greater than 10 mm from the target. However in atmosphere conditions, where plume expansion is confined by the ambient gas, expansion of emitting species is limited to a distance of $\sim$2.5 mm from the target, creating a smaller source, which is beneficial for light-collection optics in LIBS systems. Higher emission intensities are seen in the atmosphere case due to confinement, as emission is concentrated in a smaller region.

Expansion dynamics of fs LPP are significantly different from ns LPP. Instead of spherical expansion noticed in ns LPP, fs LPP plumes are found to expand with a much stronger forward bias in directions normal to the target surface, as seen in both atmosphere and vacuum cases in Fig. 6.8. Verhoff et al. [25] showed that fs LPP provided narrower angular distribution of ions and evaporated mass in comparison with ns LPPs. Like the ns LPP case in vacuum, expansion of emitting species in fs LPP can also be seen at distances greater than 10 mm, while in atmosphere, stronger emission can be seen at farther distances from the target surface in the case of fs LPP due to the pinching and cylindrical expansion of the plasma compared to ns LPP, though like ns LPP, emission is limited to a distance of $\sim$2.5 mm. Forward directed expansion of fs laser plumes can be understood by

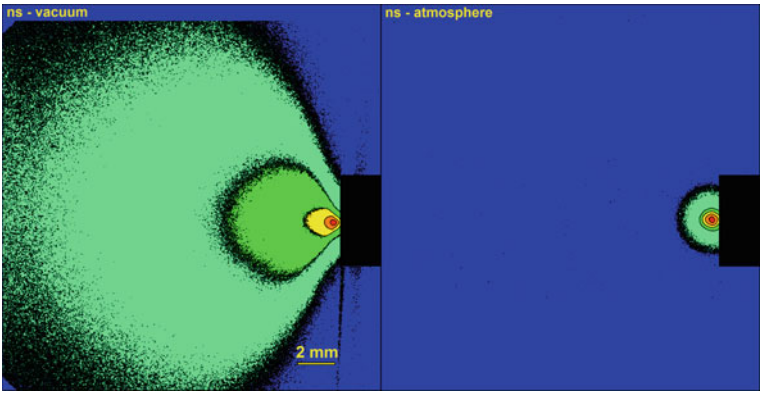

Fig. 6.7 ICCD time-integrated images of optical emission from ns LPP on brass target in vacuum and atmosphere conditions, showing spherical plume expansion. Emission intensities were normalized to the maximum observed from this figure and Fig. 6.8

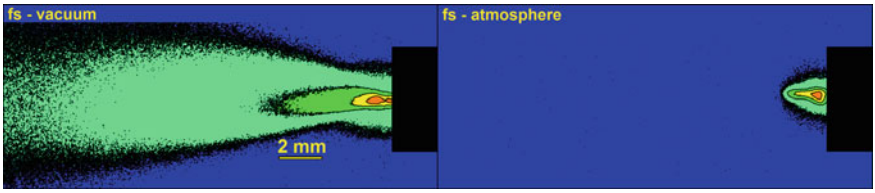

Fig. 6.8 ICCD time-integrated images of optical emission from fs LPP on brass target in vacuum and atmosphere conditions, showing cylindrical plume expansion. Emission intensities were normalized to the maximum observed from this figure and Fig. 6.7

considering pressure confinement due to strong overheating in the laser impact zone [16]. Lower visible emission intensities were observed from the fs LPP than those observed from the ns LPP despite similar laser fluence conditions [42]. In both ns and fs LPP cases, strongest emission was observed closest to the target surface, as this region of the plasma is hottest.

6.7.2 Plasma Spectral Features

The advantages offered by fs LPP in terms of figures of merit are debatable and still require further understanding of fundamentals of fs laser ablation so as to optimize the fs LPP-based analytical systems. As discussed earlier in this chapter, the major difference in plasma emission occurs due to shorter duration of laser pulse resulting in completely different mechanisms of laser-target and laser-plasma interactions and plasma expansion processes, which dictate the plasma lifetime,

plasma emission and analytical figures of merit. This is expected to result in lower excited species density, lower excitation temperatures, shorter persistence time and lower continuum emission for fs LPP as compared to ns LPP in the acquisition time scales typically employed for LIBS analysis, as has been shown in different studies [47]. Reduced continuum emission shows good promise for improving the limit of detection for major and trace elements in the sample [42] as well as the use of non-gated detectors for analysis.

Various groups have studied the time resolved evolution of continuum emission for fs LPP and compared with ns LPP [40, 42, 48]. Figure 6.9 shows emission spectra from ns and fs LPP in vacuum and atmosphere environments at different times after the laser pulse [49]. The ns LPP spectra showed significant continuum especially at times <50 ns, while the continuum emission is greatly reduced in fs LPP spectra throughout the lifetime of the plasma emission. The time-resolved spectral features given in Fig. 6.9 also shows that fs LPP spectra are dominated by excited neutrals, even at the initial times, while the ns LPP spectra are dominated by ions along with intense continuum. From the spectra, it can also be observed that the lines are less broadened and more resolved in fs LPP as compared to ns LPP. Reduced broadening of lines can be attributed to reduced electron density observed in fs LPP [47, 49]. The visible emission properties of ns and fs LA also showed dissimilarities in their lifetimes: fs LPP is short lived compared to ns LA. Hence the optimal emission integration time for LIBS varies with respect to laser pulse.

Compared to ns LPP, the fs LPP emission spectra are less influenced by ambient environment, though in vacuum the peak emission intensities occur earlier and decay quickly due to free, unimpeded expansion of the plasma plume (Fig. 6.9). However, in atmosphere the peak emission intensities occur at a later time. This is caused by increased excitation and slower expansion of the plasma plume due to confinement in the ambient environment. The strong peaks seen in the ns LPP spectra are attributed to ionic emission and are not clearly visible in the fs LPP spectra, as previously discussed. Also, neutral emission peaks that are seen clearly in the fs LPP spectra are not evident at early times in the ns LPP spectra, requiring longer delays to appear and are at lower intensities compared to the ionic emission at early times. The effect of confinement of the ambient air for ns LPP emission is similar to that for fs LPP emission. It is important to note that in both vacuum and atmosphere cases, ns LPP emission exhibits stronger persistence than fs LPP emission, with spectral features present at times much longer than those seen for fs LPP. Figure 6.10 shows another comparison of fs and ns spectral features using a Si wafer as the target for ablation at same laser fluence. Clearly, the continuum emission for fs LPP is considerably lower as compared to ns LPP. Interestingly, fs LPP is devoid of any presence of ionic species emission at the observed delay of 20 ns. The difference in spectral features can again be attributed to laser ablation mechanisms in fs LPP, which produce a plume dominated by mostly neutral species resulting from thermal vaporization. Thermal vaporization produces a mostly atomic plume, as temperatures of the emitted species are near to

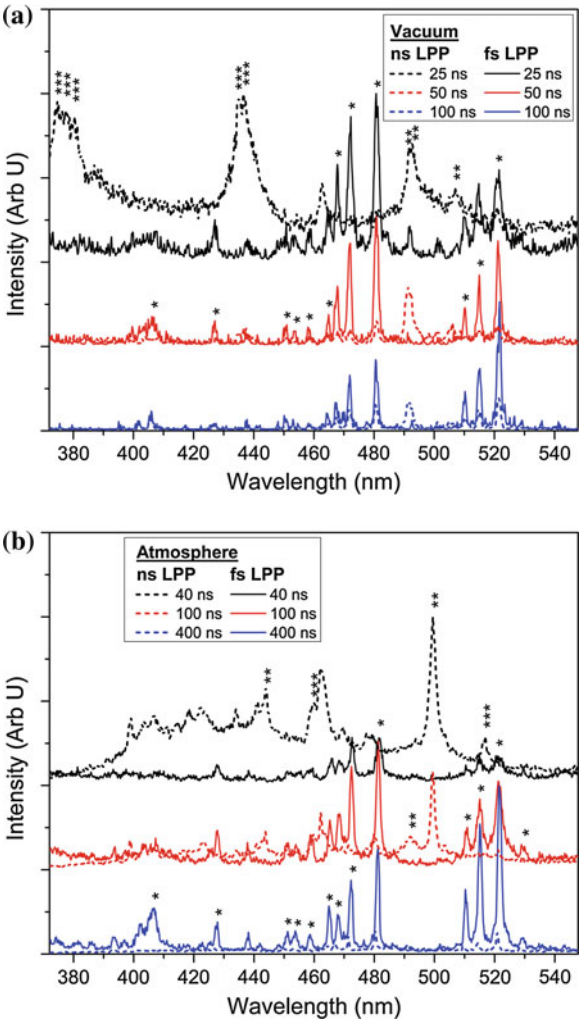

Fig. 6.9 Spectral emission from ns and fs LPP in vacuum (**a**) and atmosphere (**b**) at different gate delays, collected 1 mm from the target. Spectra have been scaled upwards for clearer viewing. Each set of three ns or fs LPP spectra were normalized to the peak intensity of that individual set for comparison of intensity fluctuations at different gate delays. (* denotes neutral line, ** denotes 1^+ ionic line, *** denotes 2^+ ionic line)

the vaporization point of the bulk and such species were far enough below the surface that ionization by the laser pulse is minimized.

Most of the studies for ns and fs LPP comparison have been performed using different laser sources, which makes direct comparison between the spectral features and analytical figures of merit very challenging. Reiger et al. [50] did not find any difference in ps and ns regime in terms of lifetime of the neutral species, except when they were very close to plasma formation threshold energy during 248 nm KrF laser ablation. They argued that the emission was dependent on energy deposited on the target rather than pulse duration. Sirven et al. [40] used 800 nm Ti:Sapphire laser source to generate ns and fs laser pulses of 1 mJ energy each by manipulating the regenerative amplifier. They found similar temporal

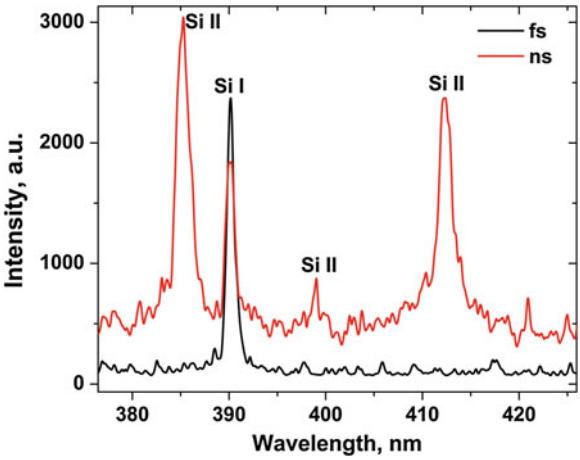

Fig. 6.10 Spectral emission from Si LIBS plume generated by ns and fs laser under similar fluence conditions. The gate delay and width of the measurement were 20 and 200 ns, respectively

emission characteristics for both neutral and ionic lines, except for ionic lines at very early moments following laser pulse arrival for fs regime. They concluded that 60–70 ns after the laser pulse, the time evolution of ionic line intensity depends strongly on laser fluence, without any significant pulse duration effects. Lower noise was observed in single shot study of fs pulses as compared to ns LPP, implying improved figures of merit for fs LPP for single shot analysis.

Yalcin et al. [51] investigated the influence of pressure on fs LPP and its implications on plasma emission. Laser pulse energies in the μJ range were used and they found significant signal enhancements in low-pressure conditions for different elements, including Al, Mg, Si and Cu. Both neutral as well as ionic lines showed a significant increase in signal with decrease in pressure with maximum emission observed at $\sim$0.85 Torr. They also studied the signal enhancement as a function of gate delay for different pressure and observed that by optimizing the delay and pressure, enhancements up to 55–67 times could be achieved for Al I lines (394.6 nm). Similar enhancements in emission have been observed for ns LPP as well, but the mechanisms are different for these cases. They attributed the enhancement in signal to optimum balancing of plasma hydrodynamic expansion and collisional excitation. Baudelet et al. [39] showed that during analysis of biological samples, fs LIBS provided less interference from ambient air emission and higher contrast for the detection of trace elements in the bacterial sample.

Ultrafast LIBS is also being used for detection of explosive residues by detecting molecular emissions of CN and C_2, which are the signature species for high energy materials [52, 53]. One of the important criteria for detection of explosives in hazardous environments is the ability of the detection technique to distinguish the signal of the explosives from the ambient, which is composed of the same elements and molecules (C, N, O). Ultrafast LIBS offers two advantages over ns LPP in this regard: minimal entrainment of atmospheric N and O and lower background emission, which makes fs LPP an attractive alternative for

explosive residue detection. It has been shown that lower laser fluence is beneficial, both in terms of figures of merit as well as cost, for optimizing the best explosive detection capability using fs LPP [53]. Spatio-temporal analysis of C_2 emission showed more uniform emission from fs LA and mainly formed due to recombination of higher charged ions and excited neutrals while multiple formation mechanisms supported by bimodal distribution are seen for ns LA [54, 55].

For quantitative analysis, it is important to improve signal to noise (S/N) of the analytical technique. Spectral acquisition delay plays an important role for optimizing the S/N or S/B (Signal to background) and precision for quantitative analysis. Freeman et al. [49] estimated S/N and S/B for fs LPP in both atmospheric pressure and vacuum conditions and noticed that in vacuum and at earlier times, the fs LPP provides improved S/N and S/B ratios. However, both S/N and S/B ratios are found to improve with respect to time when the plasmas are evolving in the presence of 1 atmosphere air. At early times after the laser pulse, S/N and S/B ratios are poor for ns LPP due to strong continuum emission dominating over the neutral line emission, especially in atmosphere, as free electrons are confined within the plume. In vacuum these values peak early in the plasma evolution as free expansion results in reduced continuum emission, while in atmosphere these values continue to increase at later times because of confinement of the plume, resulting in electron-ion recombination and hence, significantly reduced continuum emission and increased neutral emission. S/N also depends on laser pulse energy and pressure conditions as reported by Yalcin et al. [51]. They used very low laser pulse energy (10 μJ) and observed maximum S/N for zero ns delay and 1 μs integration time for atmospheric pressure conditions, while for reduced pressure conditions (4 Torr), maximum S/N was observed at later delays of 85 ns. For obtaining the best figures of merit, an optimum combination of detection window, laser pulse energy and pressure conditions are required for both ns as well as fs LPP.

6.7.3 Plasma Characterization

Plasmas produced by laser ablation contain electrons, ions, neutral particles, and clusters. The populations and dynamics of each are highly dependent on laser properties such as wavelength, pulse duration, and energy and ambient environment conditions. Pulse duration dictates the laser absorption, heating, and ablation processes as discussed in the previous sections, while laser energy can affect the magnitude at which these processes occur. Finally, ambient environment conditions can greatly affect the dynamics of the plasma plume, whether it be free expansion in vacuum or confinement and increased collisional rates and/or reactions with an ambient gas. This section provides the study of plasmas and their dynamic properties, focusing on ultrafast laser-produced plasmas and how they differ from those produced by traditional longer-pulse lasers.

Optical emission spectroscopy is one of the most powerful nonintrusive plasma diagnostic techniques to characterize the most important parameters of the plume: viz. electron temperature and electron density [56, 57]. The intensity as well as the spectral width of the emission lines can be correlated with temperature and density of the plume. For estimating electron number density as well as excitation temperature, researchers routinely use the Stark broadening of isolated line emission and Boltzmann plot employing several emission lines, respectively [42, 58, 59]. The Stark broadening method is based on the broadening of spectral lines by the presence of charged particles. The full-width half maximum (FWHM) of the spectral line, $\Delta\lambda_{1/2}$, typically fit with a Lorenzian or Voigt profile, is directly correlated to the electron number density in the plasma through an experimentally or theoretically determined electron impact width parameter, W (nm), using the following equation [59]:

$$\Delta\lambda_{1/2}(nm) = 2W\left(\frac{n_e}{10^{16}}\right) + 3.5A_i\left(\frac{n_e}{10^{16}}\right)^{5/4}\left(1 - \frac{3}{4}n_D^{-1/3}\right)W \tag{6.1}$$

where A_i(nm) is the ion broadening parameter, n_e(cm^{-3}) is the electron number density, and n_D(cm^{-3}) is the number of particles in the Debye sphere. The broadening contribution from ions is generally insignificant compared to that from electrons and the second term can be neglected.

The Boltzmann plot method uses spectral line intensities of a particular species to estimate plasma excitation temperature, assuming the plasma is in Local Thermodynamic Equilibrium (LTE). According to the Atomic State Distribution Function (ASDF) described by the Boltzmann distribution, the relative populations of excited levels of a species, and hence the corresponding spectral line intensity ratios, are characteristic of the plasma's temperature. Using the following equation [59]:

$$\ln\left(\frac{I_{ki}\lambda}{g_k A_{ki}}\right) = -\frac{1}{k_B T_{ex}}E_j + \ln\left(\frac{hcn_e}{4\pi U(T_{ex})}\right) \tag{6.2}$$

The excitation temperature can be determined from the slope of $\ln\left(\frac{I_{ki}\lambda}{g_k A_{ki}}\right)$ versus E_j, where I_{ki} is the intensity of the transition, λ is the wavelength of the transition, g_k is the degeneracy of the upper state, A_{ki} is the transition probability, k_B is the Boltzmann constant, T_{ex} is the excitation temperature, E_j is the energy of the upper state, h is Planck's constant, c is the speed of light, and $U(T_{ex})$ is the partition function. Cristoforetti et al. [60] have reported an article describing in detail the criteria for LTE required for accurate implementation of the Boltzmann plot method.

The estimated time evolution of plasma excitation temperature and electron density for ns and fs LPP employing Boltzmann plot and Stark broadening methods, respectively are given in Figs. 6.11 and 6.12 for plumes expanding into vacuum as well as in air. Confinement of the plumes in atmosphere increases the persistence of spectral lines, resulting in plasma emission lasting far longer than in

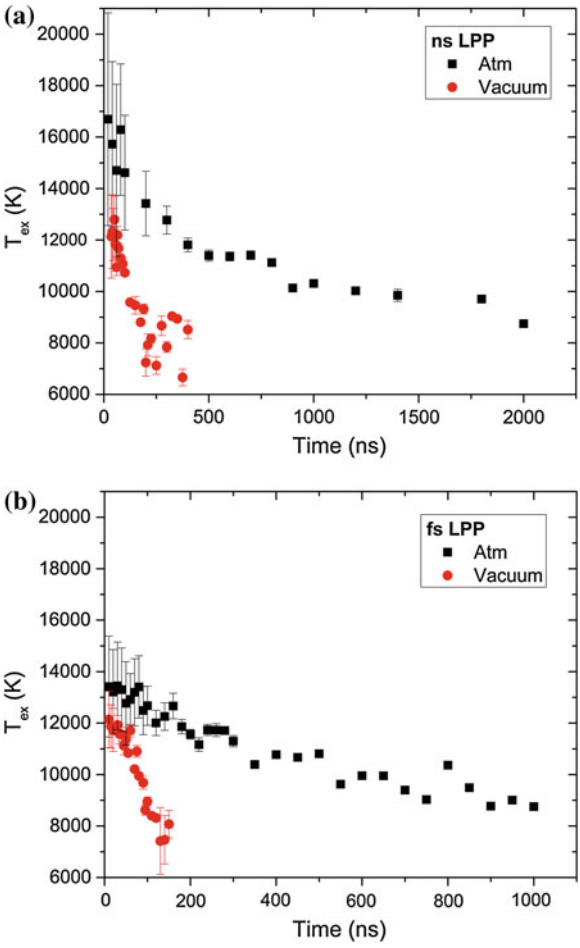

Fig. 6.11 Plasma excitation temperature evolution with time after laser pulse for ns (**a**) and fs (**b**) LPP in atmosphere and vacuum conditions from a brass target are given. The measurements were made at 1 mm from the target surface under similar laser fluence conditions (76 Jcm^{-2}). Excitation temperature estimates were made using Boltzmann plot method with error bars representing the confidence of the Boltzmann plot fitting function

vacuum, where free expansion results in faster decay [61]. Note that both ns and fs LPP both decay to similar values, though fs LPP reach these values in about half the time. At early times in ns LPP evolution, temperatures appear higher than those from fs LPP due to increased ionization and heating of the plasma during the laser pulse, an effect of plasma shielding. Temperatures from fs LPP are not as high because initial temperatures are approximately the vaporization temperature of the material. However, at very early times (<1 ns) temperature of the fs LPP, consisting of mostly energetic electrons and highly-charged fast ions as a result of the space-charge effect, is expected to far exceed that from ns LPP. Spectral emission from these electrons and ions is generally appearing in the high energy side of the electromagnetic spectrum [62, 63].

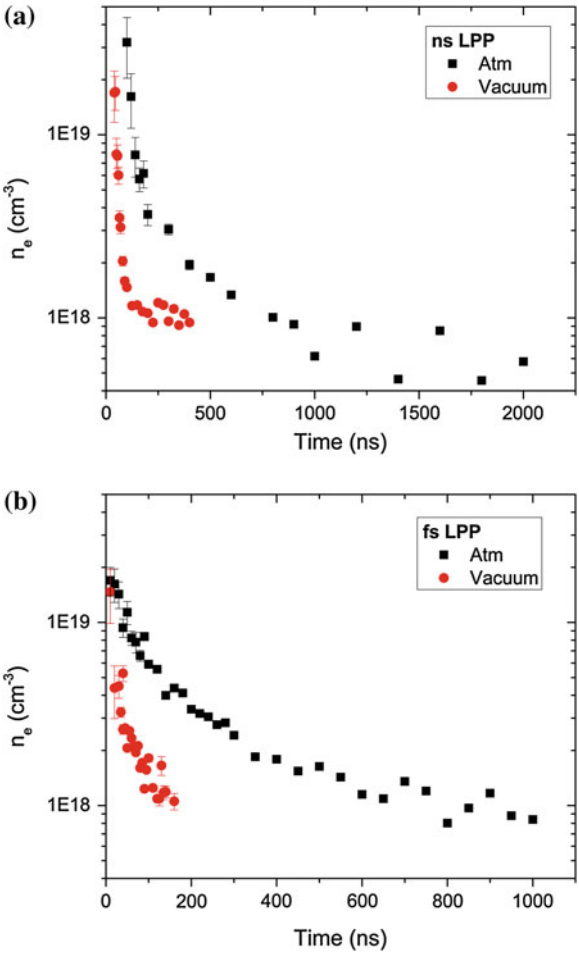

Fig. 6.12 Plasma electron density evolution with time after laser pulse for ns (**a**) and fs (**b**) LPP in atmosphere and vacuum conditions from a brass target. The measurements were made at 1 mm from the target surface under similar laser fluence conditions (76 Jcm^{-2}). Electron density estimates were made using Stark broadening technique and accounting for instrumental broadening. Error bars represent the confidence of the Lorenzian fitting function with the spectral line shape

6.8 Conclusions

Laser ablation has numerous applications and it is ever growing. Currently nanosecond lasers are routinely used for ablation and producing plasmas for various applications. The recent advancements in fs laser technology have led to a new vibrant discipline 'ultrafast optics' and directed to renewed and improved applications of laser ablation analytical techniques. Femtosecond laser ablation has showed significant improvements in ablation efficiency, less HAZ, reduced fractionation in LA-ICP-MS, insignificant continuum emission in LIBS. However, the fundamental understanding of fs-LA is still in its infancy. In this chapter, the specific details of fs laser energy transport in materials, ablation mechanisms, ablation threshold, and plume behavior are discussed in detail. A specific emphasis

is given for comparing the features of ns and fs LA and LIBS plume hydrodynamics, crater structures, ablation threshold, temperature, and density evolution.

It is too early to say that fs laser ablation will take over the position held by ns LA for various applications. However, recent results show fs laser pulses provide the best performance metrics in terms of precision, accuracy, and sensitivity for LA-ICP-MS. But, the advantages of fs-LIBS over ns-LIBS are still questionable considering the complex nature of the laser and cost. Hence the availability of user-compatible ultrafast lasers is pivotal to their widespread use in scientific research and industry. Combining key features of fs LA and considering the extensive ongoing research on turn-key femtosecond fiber and semiconductor lasers, one can easily conclude that extensive use of fs LA for various applications is imminent in near future.

Acknowledgments This work was supported by the U.S. DOE, Office of National Nuclear Security Administration (NNSA) under Award Nos. DE-NA0000463 and DE-NA0001174.

References

1. J.R. Freeman, S.S. Harilal, B. Verhoff, A. Hassanein, Plasma Sour Sci Technol **21**, 055003 (2012)
2. A. Bogaerts, Z.Y. Chen, Spectrochim. Acta B **60**, 1280 (2005)
3. D. Strickland, G. Mourou, Opt. Commun. **56**, 219 (1985)
4. A.M. Weiner, *Ultrafast Optics* (Wiley, New York, 2009)
5. R.P. Drake, *High-Energy-Density-Physics Fundamentals, Intertial Fusion and Experimental Astrophysics* (Springer, New York, 2006)
6. S. Cipiccia, M.R. Islam, B. Ersfeld, R.P. Shanks, E. Brunetti, G. Vieux, X. Yang, R.C. Issac, S.M. Wiggins, G.H. Welsh, M.P. Anania, D. Maneuski, R. Montgomery, G. Smith, M. Hoek, D.J. Hamilton, N.R.C. Lemos, D. Symes, P.P. Rajeev, V.O. Shea, J.M. Dias, D.A. Jaroszynski, Nat. Phys. **7**, 867 (2011)
7. F. Krausz, M. Ivanov, Rev. Mod. Phys. **81**, 163 (2009)
8. M. Nantel, J. Itatani, A.C. Tien, J. Faure, D. Kaplan, M. Bouvier, T. Buma, P. Van Rompay, J. Nees, P.P. Pronko, D. Umstadter, G.A. Mourou, IEEE J. Sel. Top. Quantum Electron. **4**, 449 (1998)
9. S.L. Chin, T.J. Wang, C. Marceau, J. Wu, J.S. Liu, O. Kosareva, N. Panov, Y.P. Chen, J.F. Daigle, S. Yuan, A. Azarm, W.W. Liu, T. Seideman, H.P. Zeng, M. Richardson, R. Li, Z.Z. Xu, Laser Phys. **22**, 1 (2012)
10. J.V. Moloney, in *High-Power Laser Ablation VI, Pts 1 and 2*, ed. by C.R. Phipps, vol. 6261. (Spie-Int Soc Optical Engineering, Bellingham, 2006), p. 26102
11. K. Stelmaszczyk, P. Rohwetter, G. Mejean, J. Yu, E. Salmon, J. Kasparian, R. Ackermann, J.P. Wolf, L. Woste, Appl. Phys. Lett. **85**, 3977 (2004)
12. S. Tzortzakis, D. Anglos, D. Gray, Opt. Lett. **31**, 1139 (2006)
13. H.L. Xu, J. Bernhardt, P. Mathieu, G. Roy, S.L. Chin, J. Appl. Phys. **101**, 033124 (2007)
14. H.A. Huang, L.M. Yang, J.A. Liu, Appl. Opt. **51**, 8669 (2012)
15. B. Rethfeld, K. Sokolowski-Tinten, D. von der Linde, S.I. Anisimov, Appl Phys A Mater **79**, 767 (2004)
16. E.L. Gurevich, R. Hergenroder, Appl. Spectrosc. **61**, 233a (2007)
17. M. Sabsabi, in *Laser-Induced Breakdown Spectroscopy*, eds. by J.P. Singh, S.N. Thakur (Elsevier, Amsterdam, 2007)

18. V. Zorba, X.L. Mao, R.E. Russo, Appl. Phys. Lett. **95,** 041110 (2009)
19. S.S. Harilal, G.V. Miloshevsky, T. Sizyuk, A. Hassanein, Phys. Plasmas **20**, 013105 (2013)
20. S.S. Harilal, T. Sizyuk, A. Hassanein, D. Campos, P. Hough, V. Sizyuk, J. Appl. Phys. **109**, 063306 (2011)
21. R.W. Coons, S.S. Harilal, S.M. Hassan, A. Hassanein, Appl. Phys. B **107**, 873 (2012)
22. L. Jiang and H.L. Tsai, in *Proceedings of NSF Workshop on Research Needs in Thermal, Aspects of Material Removal*, p. 163 (2003)
23. A. Kaiser, B. Rethfeld, M. Vicanek, G. Simon, Phys. Rev. B **61**, 11437 (2000)
24. R. Stoian, D. Ashkenasi, A. Rosenfeld, E.E.B. Campbell, Phys Rev B **62**, 13167 (2000)
25. B. Verhoff, S.S. Harilal, A. Hassanein, J. Appl. Phys. **111**, 123304 (2012)
26. S. Amoruso, X. Wang, C. Altucci, C. de Lisio, M. Armenante, R. Bruzzese, N. Spinelli, R. Velotta, Appl. Surf. Sci. **186**, 358 (2002)
27. T. Donnelly, J.G. Lunney, S. Amoruso, R. Bruzzese, X. Wang, and X. Ni, J. Appl. Phys. **108,** 043309 (2010)
28. Z. Zhang, P.A. VanRompay, J.A. Nees, P.P. Pronko, J. Appl. Phys. **92**, 2867 (2002)
29. S. Amoruso, X. Wang, C. Altucci, C. de Lisio, M. Armenante, R. Bruzzese, R. Velotta, Appl. Phys. Lett. **77**, 3728 (2000)
30. D. Du, X. Liu, G. Korn, J. Squier, G. Mourou, Appl. Phys. Lett. **64**, 3071 (1994)
31. M.D. Perry, B.C. Stuart, P.S. Banks, M.D. Feit, V. Yanovsky, A.M. Rubenchik, J. Appl. Phys. **85**, 6803 (1999)
32. E.G. Gamaly, A.V. Rode, B. Luther-Davies, V.T. Tikhonchuk, Phys. Plasmas **9**, 949 (2002)
33. M. Lenzner, J. Kruger, W. Kautek, F. Krausz, Appl Phys A Mater **69**, 465 (1999)
34. V. Margetic, M. Bolshov, A. Stockhaus, K. Niemax, R. Hergenroder, J. Anal. At. Spectrom. **16**, 616 (2001)
35. K.H. Leitz, B. Redlingshofer, Y. Reg, A. Otto, M. Schmidt, Physcs Proc **12**, 230 (2011)
36. E.G. Gamaly, Phys Rep Rev Sect Phys Lett **508**, 91 (2011)
37. B.N. Chichkov, C. Momma, S. Nolte, F. von Alvensleben, A. Tunnermann, Appl. Phys. A Mater. **63**, 109 (1996)
38. B. Le Drogoff, F. Vidal, S. Laville, M. Chaker, T. Johnston, O. Barthelemy, J. Margot, M. Sabsabi, Appl Opt **44**, 278 (2005)
39. M. Baudelet, L. Guyon, J. Yu, J.P. Wolf, T. Amodeo, E. Frejafon, P. Laloi, J. Appl. Phys. **99**, 084701 (2006)
40. J.B. Sirven, B. Bousquet, L. Canioni, L. Sarger, Spectrochim. Acta B **59**, 1033 (2004)
41. X. Zeng, X.L. Mao, R. Greif, R.E. Russo, Appl Phys a-Mater **80**, 237 (2005)
42. B. Verhoff, S.S. Harilal, J. Freeman, P.K. Diwakar, A. Hassanein, J. Appl. Phys. **112**, 093303 (2012)
43. R. Osellame, G. Cerullo, R. Ramponi, *Femtosecond Laser Micromachining* (Springer, New York, 2012)
44. C. Liu, X.L. Mao, S.S. Mao, X. Zeng, R. Greif, R.E. Russo, Anal. Chem. **76**, 379 (2004)
45. S.S. Harilal, N. Farid, A. Hassanein, V.M. Kozhevin, J. Appl. Phys. **114**, 203302 (2013)
46. S. Noel, J. Hermann, T. Itina, Appl. Surf. Sci. **253**, 6310 (2007)
47. B. Le Drogoff, J. Margot, M. Chaker, M. Sabsabi, O. Barthelemy, T.W. Johnston, S. Laville, F. Vidal, Y. von Kaenel, Spectrochim. Acta B **56**, 987 (2001)
48. A. De Giacomo, M. Dell'Aglio, A. Santagata, R. Teghil, Spectrochim. Acta B **60**, 935 (2005)
49. J.R. Freeman, S.S. Harilal, P.K. Diwakar, B. Verhoff, A Hassanein, Spectrochim. Acta B **87**, 43 (2013)
50. G.W. Rieger, A. Taschuk, Y.Y. Tsui, R. Fedosejevs, Spectrochim. Acta B **58**, 497 (2003)
51. S. Yalcin, Y.Y. Tsui, R. Fedosejevs, J. Anal. At. Spectrom. **19**, 1295 (2004)
52. S. Sunku, M.K. Gundawar, A.K. Myakalwar, P.P. Kiran, S.P. Tewari, S.V. Rao, Spectrochim. Acta B, **79–80**, 31 (2013)
53. F.C. De Lucia, J.L. Gottfried, A.W. Miziolek, Opt. Express **17**, 419 (2009)
54. K.F. Al-Shboul, S.S. Harilal, A. Hassanein, Appl. Phys. Lett. **100**, 221106 (2012)
55. K.F. Al-Shboul, S.S. Harilal, A. Hassanein, Appl. Phys. Lett. **99**, 131506 (2011)

56. S.S. Harilal, C.V. Bindhu, R.C. Issac, V.P.N. Nampoori, C.P.G. Vallabhan, J. Appl. Phys. **82**, 2140 (1997)
57. S.S. Harilal, B. O'Shay, M.S. Tillack, M.V. Mathew, J. Appl. Phys. **98**, 013306 (2005)
58. R.W. Coons, S.S. Harilal, M. Polek, A. Hassanein, Anal Bioanal Chem **400**, 3239 (2011)
59. H.R. Griem, *Principles of Plasma Spectroscopy* (Cambridge University Press, Cambridge, 1997), p. 19
60. G. Cristoforetti, A. De Giacomo, M. Dell'Aglio, S. Legnaioli, E. Tognoni, V. Palleschi, N. Omenetto, Spectrochim. Acta B **65**, 86 (2010)
61. N. Farid, S.S. Harilal, H. Ding, A. Hassanein, Appl. Phys. Lett. **103**, 191112 (2013)
62. M. Yoshida, Y. Fujimoto, Y. Hironaka, K.G. Nakamura, K. Kondo, M. Ohtani, H. Tsunemi, Appl. Phys. Lett. **73**, 2393 (1998)
63. U. Teubner, G. Kuhnle, F.P. Schafer, Appl. Phys. Lett. **59**, 2672 (1991)